CHEMISTRY OF MATERIALS
Cite This: Chem. Mater. 2019, 31, 4536−4544
Article
pubs.acs.org/cm

Fluorescent Ultrashort Nanotubes from Defect-Induced Chemical Cutting

Yunfeng Li,[†] Xiaojian Wu,[†] Mijin Kim, Jacob Fortner, Haoran Qu, and YuHuang Wang*

Department of Chemistry and Biochemistry, University of Maryland, College Park, Maryland 20742, United States

Supporting Information

ABSTRACT: Ultrashort single-walled carbon nanotubes (SWCNTs) that fluoresce brightly in the shortwave infrared could open exciting opportunities in high-resolution bioimaging and sensing. However, this material remains largely unexplored due to the synthetic challenge. Here, we describe a high-yield synthesis of fluorescent ultrashort nanotubes based on a fundamentally new understanding of defect-induced chemical etching of SWCNTs. We first implant fluorescent sp^3 quantum defects along the nanotube sidewalls and then oxidatively cut the nanotubes into ultrashort pieces using hydrogen peroxide. This simple two-step process leads to the synthesis of fluorescent ultrashort nanotubes with a narrow length distribution (38 ± 18 nm) and a yield as high as 57%. Despite their ultrashort length, the cut SWCNTs fluoresce brightly in the shortwave infrared at wavelengths characteristic of the sp^3 defects, which provides a spectral fingerprint allowing us to uncover new insights into this defect-induced cutting process. Quantum chemical computations suggest that this etching reaction occurs selectively at the defect sites where hydroxyl radicals ($^{\bullet}OH$) attack the surrounding electron-rich carbon atoms. This work reveals fundamental insights into defect chemistry and makes fluorescent ultrashort nanotubes synthetically accessible for both basic and applied studies of this largely unexplored but rich class of synthetic molecular nanostructures.

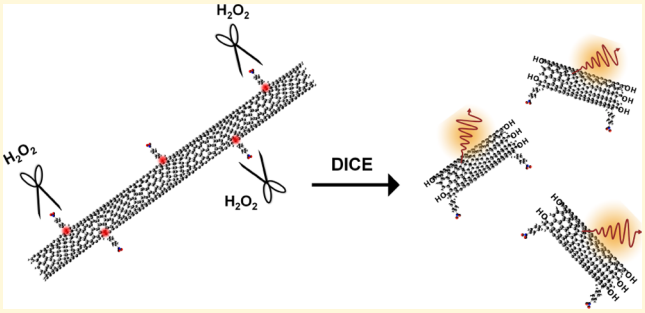

INTRODUCTION

Ultrashort single-walled carbon nanotubes (SWCNTs) that fluoresce brightly in the shortwave infrared have been a long sought-after synthetic target.[1−7] The strong motivations behind this pursuit also include an understanding of quantum confinement along the length of this family of carbon semiconductors,[3,8,9] as well as their potential use in bioimaging and biosensing applications.[10−15] Light in the second near-infrared (NIR-II) window (1000−1700 nm) can penetrate biological tissue up to centimeters in depth because of the low scattering and absorption, as well as weak autofluorescence at these wavelengths.[10] With their intrinsic NIR-II photoluminescence (PL), SWCNTs have enabled high-resolution in vivo bioimaging of blood vessels beneath the deep layers of skin,[11] extracellular space in a live brain,[12] paravertebral cells,[13] and tumors.[14] Selective detection of nitric oxide, which plays a significant role in the regulation of pulmonary vasomotor tone[16] in mice lung tissue, was also achieved using SWCNTs as in vivo photoluminescent biosensors.[15]

However, the promise of SWCNTs in bioimaging and biosensing has been severely limited by toxicity and biocompatibility concerns.[10,11,17−19] Many experiments suggest that the biotoxicity of SWCNTs can be addressed by decreasing the length of the materials to ultrashort scales (<80 nm).[17,19] For example, Kostarelos showed that short nanotubes (<1000 nm) do not react with the mesothelium of the lungs, thus preventing inflammation and granuloma in mice.[19] Moussa and colleagues also reported that well-individualized and sufficiently short (<300 nm) SWCNTs can be eliminated through the kidney and bile ducts and suggested that discrete, individual "molecule-like" ultrashort nanotubes are the key for achieving the promise of SWCNTs in bioimaging.[17] In addition to the increased biocompatibility, ultrashort nanotubes promise to significantly improve imaging resolution in the shortwave infrared due to their exceptionally small sizes. However, such materials typically do not fluoresce because of their constrained length compared with the exciton diffusion distance (>100 nm).[6,7,20] Excitons diffusing along ultrashort nanotubes unavoidably encounter the nanotube ends and nonradiatively recombine, quenching the intrinsic SWCNT PL.[6] Due to this limitation, the possibilities of ultrashort nanotubes in bioimaging and biosensing remain largely underexplored.

Our recent work demonstrates that intense PL can, in fact, be generated in ultrashort nanotubes (~40 nm) through the incorporation of fluorescent sp^3-defect sites.[6] In that study, we were able to produce a small sample of ultrashort nanotubes that were fluorescent using SWCNTs that had been previously broken into smaller segments by ultrasonication and then functionalizing them with perfluorinated hexyl functional

Received: March 26, 2019
Revised: May 23, 2019
Published: May 24, 2019

DOI: 10.1021/acs.chemmater.9b01196
Chem. Mater. 2019, 31, 4536−4544

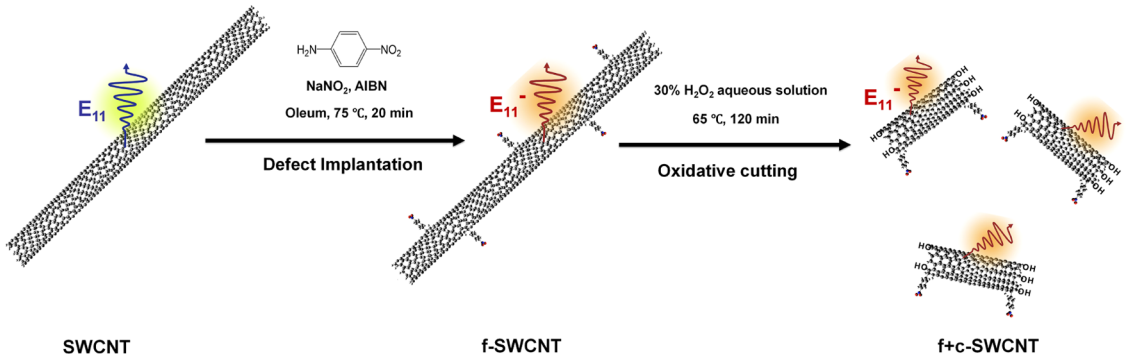

Figure 1. Schematic of DICE. This functionalize-then-cut two-step process involves (1) implanting sp^3 chemical defects along the SWCNT sidewalls by covalently attaching organic functional groups (e.g., *p*-nitroaryl as illustrated here) to form f-SWCNTs, and then (2) cutting the f-SWCNTs with H_2O_2 into ultrashort nanotubes (f + c-SWCNTs) that fluoresce in the shortwave infrared. Note that E_{11} emission is the intrinsic PL of the SWCNT, while E_{11}^- emission is the defect-induced PL in the f-SWCNT and f + c-SWCNT.

groups ($-C_6F_{13}$). Super-resolution PL imaging suggests that the implanted $-C_6F_{13}$ groups preferentially locate at the nanotube ends and can trap excitons, preventing them from encountering dangling bonds and other end defects that typically act as quenching sites. Trapping at these optically allowed defect sites allows the excitons to radiatively recombine, generating a defect-induced PL peak that is red-shifted from the native nanotube PL.[21−23] However, the synthesis of these ultrashort, fluorescent nanotubes suffers from long processing time (pulsed tip sonication at 45 W for 10 h and ultracentrifugation for 2 h), microscopic scale, and low yields (<10%). These limitations make it challenging to produce adequate samples for many experiments, such as biological imaging, where high-dose injection into live animals is usually required.[24] Therefore, a more scalable and high-yield method to synthesize these fluorescent, ultrashort nanotubes is necessary to drive forward fundamental studies and practical applications of these new materials.

From the chemistry perspective, current nanotube-cutting techniques, such as those based on tip sonication[5,25] or oxidation,[1,26,27] produce nanotubes that are not fluorescent. Additionally, ultrasonication results in a very broad nanotube length distribution (10−200 nm) and subsequently requires density gradient ultracentrifugation to purify ultrashort fractions, giving rise to severe material losses.[3,7] Strong oxidants, including piranha solution (96% H_2SO_4 + 30% H_2O_2, v/v = 4:1)[26] and a mixture of 98% H_2SO_4 and 70% HNO_3 (v/v = 3:1),[1,27] have demonstrated the capability to shorten and, in some cases, cut nanotubes by chemical oxidation. However, these methods also damage and consume the graphitic sidewalls, destroying the SWCNT electronic structure and fluorescent properties.[26,28] Although the underlying mechanism is unclear, oxidation presumably leaves behind PL-quenching defects. It is also intriguing whether defects in the graphitic sidewalls play a role in these oxidative reactions.[26,28]

To solve this synthetic challenge and address the associated fundamental questions concerning the roles of defects in oxidative chemistry, herein, we demonstrate a defect-induced chemical etching (DICE) strategy (Figure 1) that enables a scalable synthesis of fluorescent ultrashort nanotubes (FUNs). DICE is a straightforward, two-step process that involves first covalently implanting *p*-nitroaryl defects on the SWCNT sidewalls through diazonium chemistry and then cutting the nanotubes by hydrogen peroxide (H_2O_2). In the first step, the implanted *p*-nitroaryl defects not only provide preferential cutting sites for H_2O_2 and thus accelerate the cutting process but also generate a defect-induced emission peak (E_{11}^-), which is red-shifted from the nanotube's intrinsic E_{11} PL,[6,21,22] allowing us to use it as an optical fingerprint to track this reaction. In the second step, H_2O_2 selectively cuts the nanotubes from the implanted defect sites without introducing additional sidewall defects. Quantum chemical computations reveal that the *p*-nitroaryl groups introduce negatively charged, reactive sp^3-defect centers on the nanotube sp^2 lattice where H_2O_2 oxidation preferentially occurs. With this defect-selective chemistry, we were able to synthesize FUNs with a narrow length distribution (38 ± 18 nm) at a yield as high as 57% while simultaneously generating bright PL in the shortwave infrared. Our work thus lays the foundation for the scalable synthesis of FUNs, enabling further studies of this new material and their potential incorporation in bioimaging and biosensing applications.

EXPERIMENTAL SECTION

Implanting sp^3 Defects in SWCNTs. The first step of DICE is the functionalization of SWCNTs with sp^3 quantum defects. Raw CoMoCAT SG65i SWCNTs (≥99%, Lot No. SG65i-L39, SouthWest NanoTechnologies; 6 mg) were added to oleum (20% free SO_3, Sigma-Aldrich; 20 mL) and stirred to ensure that the nanotubes were well dispersed. *Safety note*: the functionalization reaction must be performed in a fume hood. Protective gloves and masks are needed when transferring oleum, which is extremely acidic and corrosive. $NaNO_2$ (analytical standard, Sigma-Aldrich; 1.725 mg) and *p*-nitroaniline (analytical standard, Sigma-Aldrich; 3.45 mg) were then added to the system, keeping the molar ratio of carbon atoms to *p*-nitroaryl groups at 20:1. The system was heated to 75 °C, and then 5.0 mg of azobisisobutyronitrile (AIBN, 98%, Sigma-Aldrich) was added as a radical initiator. After 20 min of heating and stirring, the system was removed from the hot plate. After cooling down, the oleum solution was carefully transferred to 500 mL of 2.0 M NaOH (≥97%, Sigma-Aldrich) aqueous solution, drop by drop, to neutralize the ultraconcentrated sulfuric acid until the system reached pH 8. *Note*: this neutralization step is exothermic and can produce corrosive fumes and therefore it must be done slowly in a fume hood. We then vacuum-filtrated the solution to collect the functionalized SWCNTs (f-SWCNTs), followed by rinsing the material with water and ethanol several times to remove impurities. The f-SWCNTs obtained on filter paper were dried in vacuum for 1 h.

Cutting f-SWCNTs in H_2O_2. The second step of DICE is cutting f-SWCNTs in H_2O_2. f-SWCNTs (2 mg) were homogenized in 10 mL of deionized water (Milli-Q water) with 1 wt % sodium deoxycholate (DOC, ≥98%, Sigma-Aldrich) by bath sonication for 30 min. H_2O_2

DOI: 10.1021/acs.chemmater.9b01196
Chem. Mater. 2019, 31, 4536−4544

(10 mL, 30 wt % in H_2O, Sigma-Aldrich) was then added and mixed well with the SWCNT surfactant dispersion. The solution was then heated to 65 °C using an oil bath while magnetically stirred until the SWCNTs were totally digested and the solution became transparent. Functionalized and cut SWCNT (f + c-SWCNT) samples were collected every 30 min for characterization. Four fractions of samples were collected at 30, 60, 90, and 120 min. *Safety note*: H_2O_2 aqueous solution is oxidative and corrosive; avoid exposure to skin and eyes.

Alternative Approach of Defect Implanting for DICE by Commercially Available Aryl Diazonium Salts in Aqueous Solution. We dispersed 1.0 mg of raw CoMoCAT SG65i SWCNTs in 10 mL of D_2O (99.8 atom % D, Cambridge Isotope Laboratories, Inc.) with 1 wt % of sodium dodecyl sulfate (SDS, Sigma-Aldrich) by tip sonication at 4 W for 30 min. We then diluted the stock solution using D_2O until the (6,5) nanotube optical density at E_{11} equals 0.364. 4-Nitrobezenediazounium tetrafluoroborate powder (7.72 mg, Sigma-Aldrich, 97%) was dissolved in 1 mL of D_2O, followed by serial dilution (dilution factor = 1:1000). We added 250 μL of this diluted solution to 2 μL of the dispersed SWCNTs in SDS/D_2O solution in a cuvette and then illuminated the solution with 565 nm light using a NanoLog spectrofluorometer (Horiba Jobin Yvon) while stirring the sample using a magnetic bar. We monitored the reaction in real-time-control mode and terminated the reaction by turning off the laser when the E_{11}^- peak (~1150 nm) became stable. This process was repeated five times to prepare ~10 mL solution of f-SWCNTs.

We then added 5 mL of H_2O_2 (30 wt % in H_2O) to 5 mL of the prepared f-SWCNTs in SDS/D_2O solution. The solution was then heated to 65 °C using an oil bath while being magnetically stirred. The resulting f + c-SWCNT samples were collected after 2 h of oxidative cutting with H_2O_2.

Spectroscopic Characterization. UV−vis−NIR absorption spectra were collected by a spectrophotometer with a broad-band InGaAs detector (Lambda 1050, PerkinElmer). To calculate the yield, f-SWCNTs before and after oxidation were dispersed in 4 mL of 1 wt % DOC in H_2O.

The PL spectra and two-dimensional (2D) excitation−emission PL map were collected on the NanoLog spectrofluorometer. To exclude effects of H_2O_2 on the PL, we added 8 μL of 8 mg $Na_2S_2O_4$ (technical grade, Sigma-Aldrich)/0.1 mL of D_2O solution to quench residual H_2O_2, followed by adding a few microliters of 8 mg $NaHCO_3$ (≥99.7%, Sigma-Aldrich)/0.1 mL of D_2O aqueous solution until the system was weakly basic (pH ~ 8). The samples were excited with a 450 W xenon source dispersed by a double-grating monochromator. The slit widths of the excitation and emission beams were 10 nm. The PL spectra were collected using a liquid-N_2-cooled linear InGaAs array detector. Note that all samples had an optical density at the E_{11} band of 0.10. The integration times for the PL spectra and 2D map were 2 and 5 s, respectively. Samples were diluted in D_2O to avoid the absorption of H_2O at ~1200 nm.

Raman spectra were recorded from 150 to 3000 cm^{-1} using a LabRAM ARAMIS Raman microscope (Horiba Jobin Yvon) with a 633 nm excitation. The integration time was 0.8 s, taken 10 times in total. The power density of the incident laser was 1.2 mW/μm^2.

Fourier transform infrared (FT-IR) spectra of both pristine SWCNTs and f + c-SWCNTs (120 min of H_2O_2 oxidation) were collected using a thermal Nicolet NEXUS 670 FT-IR with an attenuated total reflection attachment.

Atomic Force Microscopy (AFM). For AFM characterization, we drop-cast the SWCNT solutions on freshly cleaved mica surfaces and allowed the droplet to remain on the substrate for 5 min, after which it was blown off using air. Then, the substrate was gently rinsed with water and ethanol in sequence to remove surfactant and other impurities, followed by blowing the sample dry with air. We imaged the substrate using AFM probes with a tip radius of less than 5 nm (TAP 300GD-G AFM probe from BudgetSensors) in the AC-air mode of an Asylum Cypher ES AFM system. We obtained topography images at a sampling rate of 0.8 Hz and a 512 line resolution. We measured more than 100 nanotubes for each sample to analyze the length distributions using Gwyddion software. The nanotube length follows the normal distribution, and we report the distributions as $\mu \pm \sigma$ in the discussions, where μ is the mean and σ is the standard deviation. In the correlated study of the AFM and PL images in the same region of interest, we used the same method to prepare the sample, though the substrate was changed to a polystyrene−Au−Si wafer substrate for PL imaging. We located the same region of the sample for correlated AFM/PL analysis using fluorescent markers on the substrate.

Control Experiment: Cutting Pristine SWCNTs in H_2O_2. To study the effect of implanted defects on oxidation, we compared the cutting efficiency of f-SWCNTs by applying the same cutting strategy to pristine SWCNTs. CoMoCAT SG65i SWCNTs (2 mg) were homogenized in 10 mL of 1 wt % DOC/H_2O by bath sonication for 30 min. H_2O_2 (10 mL of 30%) was then added and mixed well with the SWCNT solution, followed by heating at 65° C while stirring. We collected the cut pristine nanotubes after 2 h and analyzed the AFM height images. We also collected the cut pristine nanotubes after 2, 4, 6, and 8 h oxidation and measured the 2D excitation−emission PL map of these samples with integration times of 1 s.

Control Experiment: Piranha Solution Oxidation Cutting Method. Dry SWCNT powder (2 mg) was collected and well dispersed in 2 mL of oleum. Piranha solution (10 mL, 98% H_2SO_4 + 30% H_2O_2, v/v = 3:1) was then prepared with caution in an ice bath. We added the f-SWCNT/oleum solution slowly to the piranha solution in a 30 mL vial. The solution was heated up to 65 °C on a hot plate and magnetically stirred. After 30 min oxidation, we removed the vial from the heat source and neutralized the solution by slowly adding it to an excess amount of NaOH aqueous solution (2.5 M), followed by filtering the oxidized f-SWCNTs. *Note*: piranha solution and oleum are highly oxidative and acidic, protective gloves and masks are required, and skin and eye contact should be avoided.

NIR PL Imaging. The f + c-SWCNT solution (5 μL) was spread and then dried on a polystyrene-coated Au-on-Si wafer substrate. The ultrashort nanotubes were imaged with a custom-built shortwave infrared imaging system using an IR-optimized objective (Olympus LCPLN100XIR, NA 0.85) and a liquid-nitrogen-cooled InGaAs detector (Cougar-640-LN2, Xenics, Belgium). The sample was excited with a 730 nm laser at intensities kept below 64 W/cm^2 to avoid nonlinear effects. Note that this off-resonant excitation generates E_{11} excitons in (6,5)-SWCNTs and does not directly excite the emissive defects. To obtain the locations of emissive defects, we recorded a 10 min image sequence of the blinking defect emission by placing a 1100 nm long-pass filter before the InGaAs detector. The image sequence was analyzed to retrieve the super-resolved defect locations, as we previously reported.[6,29]

Geometry Optimization and Natural Population Analysis. The density functional theory (DFT) calculations were performed using Gaussian 09 software.[30] We used a 4 nm long (6,5)-SWCNT with open ends terminated by hydrogens. To model an f-SWCNT, we introduced a *p*-nitroaryl paired with a hydrogen group in the middle of the (6,5)-SWCNT. Geometry optimization was performed with the B3LYP functional and 3-21G basis set. The B3LYP functional is widely used to predict the electronic and optical properties of large organic molecules. For f + c-SWCNTs where aryl defects are covalently bound to the nanotube, B3LYP produces results that are qualitatively consistent with calculations made using larger DFT functional because the orbital localization properties are much less sensitive to the long-range corrections. The 3-21G level of theory is suitable to obtain the optimized geometries of the covalently functionalized nanotube systems and their electronic structures. To determine the partial atomic charges, we performed natural population analysis[31] on the geometrically optimized model using the NBO 3.1 software included in Gaussian 09. As the charges found from natural population analysis should converge as the basis set quality increases, we also performed the DFT optimization at the B3LYP/6-31G level to show that using a larger basis set has minimal effect on the calculated charges (Table S1).

DOI: 10.1021/acs.chemmater.9b01196
Chem. Mater. 2019, 31, 4536−4544

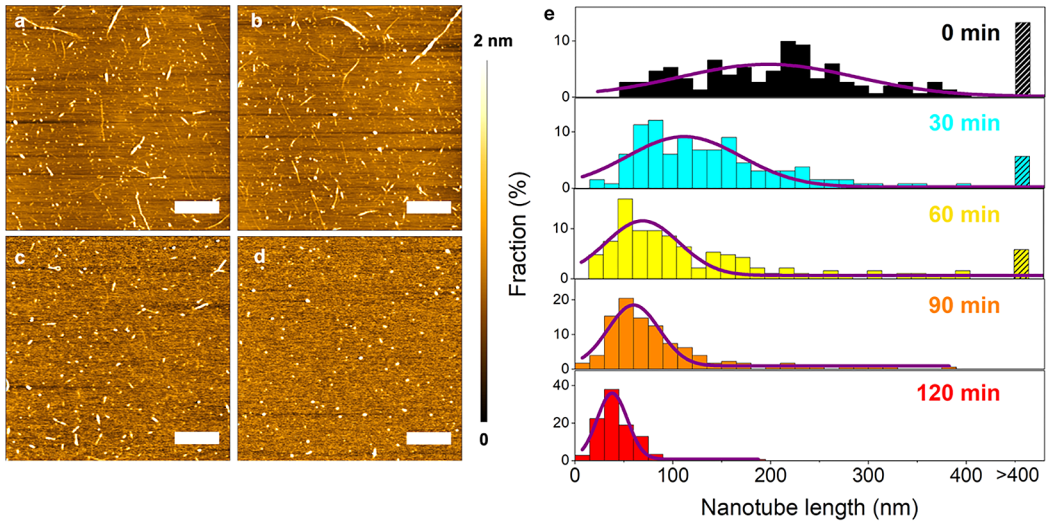

Figure 2. DICE cuts long nanotubes into ultrashort pieces with a narrow distribution of lengths. Representative AFM height images of f + c-SWCNTs with different oxidation times: (a) 30 min, (b) 60 min, (c) 90 min, and (d) 120 min. The nanotubes were deposited on mica surfaces. Scale bars: 1 μm. (e) Histograms of the length distributions of f-SWCNTs (0 min) and f + c-SWCNTs after 30, 60, 90, and 120 min oxidation. Lengths larger than 400 nm were combined into one bin (dark slashed bar).

RESULTS AND DISCUSSION

Our DICE strategy begins by covalently implanting *p*-nitroaryl groups on the sidewalls of pristine, long SWCNTs. This step can be achieved using diazonium chemistry in oleum,[32] although this step should be achievable with other chemistries.[22,33] Then, we homogenize these f-SWCNTs in 1 wt % DOC/H_2O, followed by adding H_2O_2 and heating at 65 °C to cut the nanotubes by chemical oxidation. H_2O_2 is unstable at this temperature and spontaneously decomposes to hydroxyl and hydroperoxyl radicals, which can oxidize nanotube carbon.[34,35] We hypothesized that these free radicals would selectively oxidize the more reactive sp^3-defect sites implanted at the first step of the synthesis to cut the long f-SWCNTs into shorter pieces, and this hypothesis is supported by both our experimental results and quantum chemical simulations, which will be discussed later. After this two-step functionalize-then-cut process, we obtain ultrashort nanotubes with implanted *p*-nitroaryl defects that emit at ~1150 nm, characteristic of the *p*-nitroaryl defects.[6,21,22]

DICE Cuts Long Nanotubes into Ultrashort Pieces with Narrow Length Distribution. We first investigated the effect of the H_2O_2 oxidation time on the length distribution of the f + c-SWCNTs by collecting a sample from the reaction every 30 min and characterizing it using AFM. Figure 2a–d shows the representative height images of the f + c-SWCNTs made with varying oxidation times (see also Figure S1a,b for the uncut f-SWCNT control). We randomly sampled >100 nanotubes from each fraction and plotted a stacked 2D histogram of the SWCNT length distribution in Figure 2e. Without oxidation, the f-SWCNTs featured a normal length distribution of 197 ± 106 nm (Figure S1a,b). Meanwhile, f + c-SWCNT samples with oxidation times of 30, 60, 90, and 120 min showed normal length distributions of 112 ± 69, 70 ± 44, 60 ± 31, and 38 ± 18 nm, respectively, in which we observed decreasing average length and narrowing size range with increased oxidation time. The system began with a disordered mixture of long and short nanotubes, but after 120 min, it ended with only ultrashort nanotubes that featured a narrow distribution of lengths.

Our DICE strategy is significantly more efficient at producing ultrashort nanotubes compared to the tip sonication method.[5,25] While a 2 h tip sonication at 4 W shortened the average length of the f-SWCNTs from 197 to 137 nm (Figure S1), DICE produced f + c-SWCNTs that were 38 ± 18 nm in length for the same processing time (Figure 2d,e). Additionally, the tip-sonicated sample contained a considerable fraction of long nanotubes (>200 nm: ~38%, Figure S1d), but none were observed in the DICE sample. Clearly, our DICE strategy produces shorter nanotubes with a much narrower length distribution.

An important observation from DICE is that the *p*-nitroaryl defects accelerate the oxidative cutting of f-SWCNTs. We performed the same cutting experiment with pristine nanotubes as a control (see the Experimental Section for details). After 2 h oxidation, for the nonfunctionalized control, the nanotubes were shortened from 193 ± 98 nm to just 119 ± 81 nm, and a large portion of the long nanotubes remained (>200 nm: ~30%, Figure S2). This is in stark contrast with the f + c-SWCNTs, which achieved a length distribution of 38 ± 18 nm (Figure 2e) after the same 2 h oxidation, with nearly all nanotubes converted into ultrashort materials. This acceleration effect supports our hypothesis that the oxidation reaction selectively occurs from more reactive defect sites. In pristine nanotubes, H_2O_2 only etches from the nanotube ends,[35] while in f-SWCNTs, our results suggest that oxidation preferentially cuts the nanotubes into shorter pieces at the defect sites.

DICE Retains the Electronic Structure of the Starting Nanotubes and Achieves High Yield. The electrical and optical properties of SWCNTs are substantially affected by defects or functional groups;[36,37] so, it is critical to keep the nanotube graphitic structure intact as much as possible during the oxidation process. Figure 3a shows the Raman spectra of the f + c-SWCNTs with different oxidation times. The results show that the integrity of the nanotube radial breathing modes (RBMs) is not affected by the cutting process, suggesting that the basic nanotube structure remains undamaged during exposure to H_2O_2. The G peak located at ~1580 cm^{-1} arises from the stretching of the sp^2 C–C bonds in graphitic

DOI: 10.1021/acs.chemmater.9b01196
Chem. Mater. 2019, 31, 4536–4544

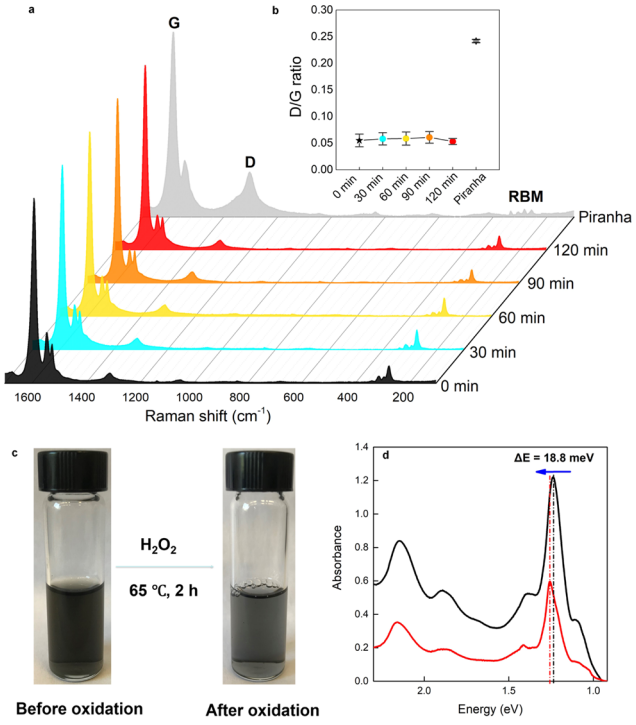

Figure 3. DICE retains the electronic structure of the starting nanotubes and achieves high yields. (a) Raman spectra of f + c-SWCNTs with different oxidation times of 0, 30, 60, 90, and 120 min. The excitation line is 633 nm. We included f-SWCNTs cut by piranha solution for 30 min for comparison. (b) Comparison of the D/G ratios of these samples. (c) Images of the f-SWCNT solution before and after the H_2O_2 cutting process for 120 min (both samples were dispersed in 4 mL of 1 wt % DOC/H_2O). (d) UV−vis−NIR absorption spectra of the f-SWCNTs before (black) and after (red) 120 min H_2O_2 oxidation.

materials, and the D peak located at ∼1310 cm^{-1} is caused by the presence of disorder (i.e., sp^3 carbon), with the ratio of the D/G peaks being conventionally used to quantify the SWCNT structural integrity.[38] Figure 3b summarizes the change of the D/G ratio of the f + c-SWCNTs as a function of oxidation time. The D/G ratio remains very low and constant (∼0.05) even with prolonged oxidation, indicating no increase in the total number of defects as a result of H_2O_2 cutting. These results agree with the cutting mechanism we have proposed, in which H_2O_2 cuts f-SWCNTs selectively from the defect sites, leaving oxygen-containing groups on the ends of the f + c-SWCNTs, while introducing no sidewall damage during cutting.

We also investigated the oxidative cutting of f-SWCNTs using piranha solution (see the Experimental Section for details). Piranha solution also cuts the f-SWCNTs, but the chemical reaction severely damages the nanotube electronic structure. In Figure 3a,b, we observed a significant increase in the D/G ratio from 0.05 to 0.25 and the deformation of the RBMs after applying piranha solution to the same f-SWCNTs. This is consistent with the previous work by Ziegler et al., which showed that the Piranha reaction introduces a large number of oxygen-containing defects as well as vacancies along the nanotube sidewalls,[39] resulting in the loss of the SWCNT electronic structure and thus quenching the PL in these samples.[26] In our case, the loss of both the E_{11} and E_{11}^- PL (Figure S3) unambiguously confirms that the piranha reaction is so aggressive that the defect PL does not survive. In contrast, H_2O_2 enables controllable cutting, which is critical for keeping both the electronic structure of the nanotubes and the aryl functional groups intact.

Importantly, DICE achieves a high yield in synthesizing FUNs from SWCNTs. In Figure 3c, we compared the f-SWCNT solution before and after 120 min H_2O_2 oxidation. The color of the solution becomes lighter after DICE due to carbon consumption during the etching process. To determine the yield, we measured the UV−vis−NIR absorption spectra of the samples before and after oxidation (Figure 3d). Because the absorbance of (6,5) SWCNT is proportional to the number of carbon atoms,[9,40] the yield of DICE can be evaluated from changes in the E_{11} absorption band,[41,42] and we obtained a yield as high as 57% for converting SWCNTs into FUNs. It is worth noting that the E_{11} absorption peak blue-shifted 18.8 meV after a 120 min oxidative cutting, which may be attributed to the quantum confinement of E_{11} excitons due to the reduced nanotube size.[4,5,7,43]

Bright PL from Ultrashort Nanotubes in the Short-wave Infrared. The ultrashort nanotubes prepared by DICE maintain the E_{11} absorption features characteristic of SWCNTs (Figure 3d), indicating that this controllable cutting process keeps the electronic structure of the ultrashort nanotubes intact. In the excitation−emission PL map of the f + c-SWCNTs (120 min H_2O_2 oxidation) (Figure 4a), we observed E_{11} PL at 980 nm and E_{11}^- PL at 1150 nm from (6,5) nanotubes, which resonate with the same excitation wavelength of 580 nm, consistent with the brightening mechanism in which mobile excitons are trapped and locally emit as the defect-induced E_{11}^- PL.[6,21,22] As proposed in Figure 1, E_{11} PL originates from the intact nanotube segments, which make up the body of the FUNs, and E_{11}^- PL is due to the added *p*-nitroaryl defects. We note that the DICE strategy applies to large diameter nanotubes as well, whose PL are weaker but can become visible by decreasing the intensity scale, as shown in Figure S4. As a control, we measured the PL of nanotubes synthesized by oxidatively cutting long pristine nanotubes in H_2O_2 for 2, 4, 6, and 8 h (see the Experimental Section and Figure S5 for details) and found that the E_{11} PL became weaker as the oxidation proceeded, while no E_{11}^- PL was observed, which allowed us to conclude that the defect-induced E_{11}^- fluorescence observed in FUNs was indeed caused by the implanted *p*-nitroaryl defects. We also found that both E_{11} and E_{11}^- PL intensities of the f + c-SWCNTs decreased with oxidation time (Figure 4b). This decrease can be attributed to the consumption of the SWCNTs.[44]

We further studied the PL at the individual nanotube level and performed single nanotube PL imaging of f + c-SWCNTs (120 min H_2O_2 oxidation). The nanotubes were dispersed in surfactant and drop-cast onto a polystyrene−Au−Si wafer substrate. The sample was then placed under an inverted microscope equipped with a liquid-nitrogen-cooled InGaAs detector. We collected the broad-band (900−1600 nm) PL images of individual nanotubes (Figure 4c) and observed bright PL from the sample, in which all fluorescent nanotubes appear as diffraction-limited spots. Due to the diffraction limit of optical microscopy, we cannot determine the length of these ultrashort SWCNTs based on the PL images. However, the defect location along the nanotube length can be determined by super-localization analysis, as we recently reported.[6] Figure 4d exemplifies a single ultrashort nanotube with two super-resolved defect sites separated by 34 nm. Figure S6 shows a histogram constructed from the statistical analysis of 20

DOI: 10.1021/acs.chemmater.9b01196
Chem. Mater. 2019, 31, 4536−4544

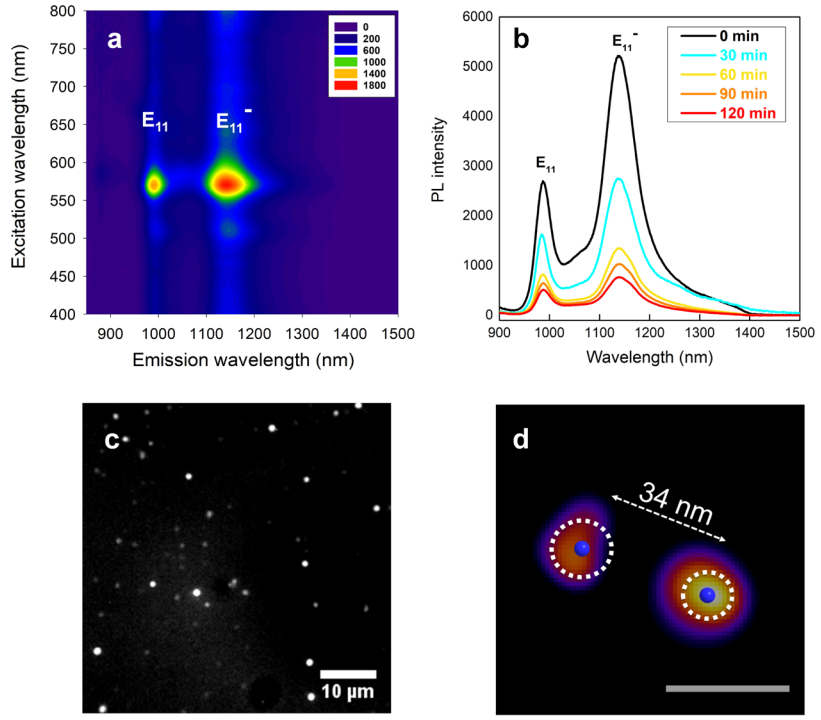

Figure 4. Bright PL from ultrashort nanotubes in the shortwave infrared. (a) Excitation−emission 2D PL map of the f + c-SWCNTs (120 min H_2O_2 oxidation) reveals the material's bright PL. (b) PL spectra of the f + c-SWCNTs made using different oxidation times (0, 30, 60, 90, and 120 min). (c) Broad-band (900−1600 nm) PL images of f + c-SWCNTs (120 min H_2O_2 oxidation). All bright spots are diffraction-limited. (d) PL image of an ultrashort nanotube with defect locations super-resolved. Scale bar = 30 nm. The mean localization of a single defect is represented by a blue spot and the corresponding localization precision (∼10 nm) by dotted circles.

nanotubes, which gives a distance of 48 ± 8 nm between two defects. This distance approximately matches the nanotube length obtained from AFM (Figure 2e), suggesting that the defects are located at the nanotube ends. This observation is in good agreement with the proposed cutting mechanism that oxidation preferentially takes place from implanted defect sites on the nanotube sidewalls, leaving *p*-nitroaryl groups on the ends of the cut nanotubes, which produce the observed defect PL.

FT-IR spectroscopy also provides chemical information supporting this conclusion. Figure S7 shows the IR spectrum of the f + c-SWCNTs (120 min H_2O_2 oxidation). We observed O−H stretching (3650−2900 cm^{-1}) and O−H bending at 1440−1395 and 1420−1330 cm^{-1} for carboxylic acid and alcohol, respectively. We also observed C−H stretching of aldehyde (2830−2695 cm^{-1}). The peak at approximately 1750−1550 cm^{-1} may include C═O stretching of an aldehyde (1740−1720 cm^{-1}), carboxylic acid (1720−1700 cm^{-1}), and ketone (1685−1666 cm^{-1}). We also noticed a broad peak of 1500−1250 cm^{-1}, which covers the N−O stretching (1550−1475 cm^{-1}, asymmetrical; 1360−1290 cm^{-1}, symmetrical) of the *p*-nitroaryl group, although the overlap with C−O stretching (1300−1250 cm^{-1}) makes it difficult to unambiguously assign this peak. We note that the chemical signatures of oxidized carbon nanotubes may be better resolved by near-edge X-ray absorption fine structure spectroscopy.[28] However, FT-IR spectroscopy supports that DICE introduces oxygen-containing groups into FUNs, such as hydroxyls (−OH), aldehydes (−CHO), ketones (−C═O), and carboxylic acids (−COOH), while the *p*-nitroaryl group survives the DICE chemistry, as indicated by the characteristic defect PL.[21,22]

To completely rule out the possibility that the observed PL may come from a small fraction of long nanotubes, we correlated AFM and hyperspectral PL imaging at the single nanotube resolution by targeting the same region of interest on the sample substrate with the aid of fluorescent markers (Figure S8). The PL image is shown in Figure S8c along with a large-area AFM image locating the same area (Figure S8d). We further zoomed in on a smaller region of this same area (5 μm × 5 μm red boxes shown in Figure S8c,d, the same region) and characterized it by AFM in tapping mode. As shown in Figure S8e, no long SWCNTs were observed; however, there were indeed several ultrashort SWCNTs, which correlate well with the PL image, confirming that the ultrashort SWCNTs produced by DICE are intensely fluorescent.

Alternative Defect-Implanting Chemistry for DICE. We found that the defects for DICE can also be implanted by off-the-shelf diazonium salts in aqueous solution, demonstrating significant generality of our strategy. After the defect-implanting diazonium reaction in aqueous solution, the f-SWCNTs emit both E_{11} PL (intrinsic) at ∼980 nm and E_{11}^- PL (defect-induced) at ∼1150 nm (Figure S9a). After a 2 h oxidative cutting in H_2O_2, the f + c-SWCNTs retain their E_{11} and E_{11}^- PL (Figure S9b). AFM measurements confirm that the carbon nanotubes were cut into short pieces (Figure S9c,d).

Quantum Chemical Computation Suggests that DICE Follows Charge-Enhanced Reactivity at the Defect Site. DICE features a highly selective cutting process induced by the introduction of sp^3-defect centers. The observed low-defect levels of the synthesized FUNs, high yield, and acceleration of nanotube cutting all consistently provide evidence that chemical cutting occurs selectively from these defect sites.

DOI: 10.1021/acs.chemmater.9b01196
Chem. Mater. 2019, 31, 4536−4544

To better understand the high selectivity of DICE, we used natural population analysis[31] to determine the charge distribution along the f-SWCNTs (see the Experimental Section for more details) and present the results in Figure 5.

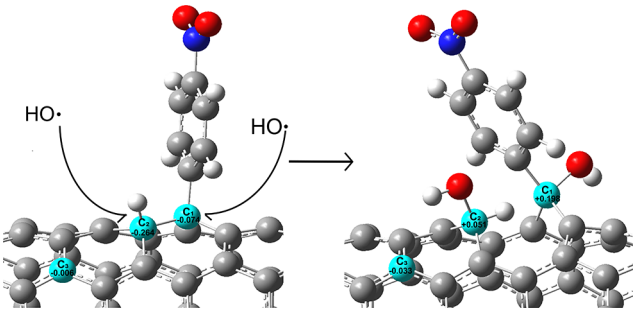

Figure 5. Quantum chemical computation suggests DICE follows charge-enhanced reactivity at the defect site. Natural population analysis shows charge distributions at the vicinity of a defect. Carbons of interest are highlighted and labeled C_1−C_3. Before the addition of hydroxyl groups, in the f-SWCNT, the sp^3 carbons at the defect site, C_1 and C_2, are negatively charged, while nearby carbons are effectively neutral. A hydroxyl radical will therefore selectively oxidize the defect site. After the addition of hydroxyl groups, C_1 and C_2 at the defect site acquire positive charges. Meanwhile, close to the defect, C_3 acquires a negative charge, making it a more favorable site for further oxidative cutting.

Note that C_1 is the sp^3-defect center connected to the *p*-nitroaryl functional group, and C_2 is another sp^3 carbon atom next to C_1, connected to a hydrogen atom. While most of the carbons in the nanotube sidewall are close to neutral in charge ($|q| < 0.03$), we found that the charges of C_1 and C_2 are −0.074 and −0.264, respectively. The negative charges of C_1 and C_2 make the sp^3 carbons more reactive during oxidation as enriched free electrons largely favor oxidation attacks by hydroxyl radicals. We propose that the oxidation of the f-SWCNT at the defect site breaks the bond between C_1 and C_2, followed by adding hydroxyl groups to both carbon atoms. We then applied natural population analysis to this new model after bond breakage and the addition of hydroxyl groups, which showed that C_1 and C_2 become positively charged (0.198 and 0.051, respectively). In return, some of the carbon atoms surrounding the defect site now gain a negative charge (e.g., C_3, −0.033), which makes them more favorable targets for further oxidative cutting. This picture shows that the initially introduced *p*-nitroaryl group stays connected to C_1, which becomes an end atom of the resulting ultrashort nanotube. Figure S10 shows more detailed natural charge distribution maps for atoms near a defect site.

CONCLUSIONS

We have addressed the synthetic challenge of fluorescent ultrashort nanotubes by implanting sp^3 chemical defects along the lengths of SWCNTs and subsequently cutting the structure at these defect centers with H_2O_2. We show that the introduced sp^3 defects not only accelerate the cutting process but also enable the ultrashort nanotubes to fluoresce brightly in the shortwave infrared despite being significantly shorter than the diffusion length of excitons. The cut SWCNTs are ultrashort and feature a narrow length distribution (38 ± 18 nm) and low-defect densities (D/G ∼ 0.05). The chemistry is highly defect-selective, as shown by its high yield (∼57%) and natural population analysis of the material's charge distribution. This work makes FUNs available at synthetic quantities, opening opportunities for bioimaging, biosensing, and photophysics, as well as other applied and fundamental studies of fluorescent ultrashort nanotubes.

ASSOCIATED CONTENT

Supporting Information

The Supporting Information is available free of charge on the ACS Publications website at DOI: 10.1021/acs.chemmater.9b01196.

Characterization of FUNs via PL spectroscopy and imaging, AFM, FT-IR spectroscopy, and correlated AFM and PL imaging; results from the control experiments including studying p-SWCNTs cut by H_2O_2 via AFM and PL spectroscopy, f-SWCNTs cut by piranha solution via PL spectroscopy; natural population analysis using different basis sets (PDF)

AUTHOR INFORMATION

Corresponding Author

*E-mail: yhw@umd.edu.

ORCID

Yunfeng Li: 0000-0003-3906-4389
Mijin Kim: 0000-0002-7781-9466
Haoran Qu: 0000-0003-4536-6703
YuHuang Wang: 0000-0002-5664-1849

Author Contributions

†Y.L. and X.W. contributed equally to this work.

Notes

The authors declare no competing financial interest.

ACKNOWLEDGMENTS

The authors thank A. H. Brozena, P. Wang, and J. A. Klos for valuable discussions. M.K. acknowledges the Millard and Lee Alexander Fellowship in Chemistry from the University of Maryland. Y.L. and X.W. are partially supported by the Center for Enhanced Nanofluidic Transport (CENT), an Energy Frontier Research Center funded by the U.S. Department of Energy, Office of Science, Basic Energy Sciences under Award # DE-SC0019112 to apply FUNs as a model system for fundamental studies of nanofluidic transport. Funding for the AFM-shared facility used in this research was provided by the NSF MRI program under award number CHE-1626288. The work also made use of instrumentation funded by NIH/NIGMS R01GM114167. Any opinion, findings, and conclusions or recommendations expressed in this material are those of the authors and do not necessarily reflect the views of the funding agencies.

REFERENCES

(1) Liu, J.; Rinzler, A. G.; Dai, H.; Hafner, J. H.; Bradley, R. K.; Boul, P. J.; Lu, A.; Iverson, T.; Shelimov, K.; Huffman, C. B.; Rodriguez-Macias, F.; Shon, Y. S.; Lee, T. R.; Colbert, D. T.; Smalley, R. E. Fullerene pipes. *Science* **1998**, *280*, 1253−1256.

(2) Chen, Z.; Kobashi, K.; Rauwald, U.; Booker, R.; Fan, H.; Hwang, W. F.; Tour, J. M. Soluble ultra-short single-walled carbon nanotubes. *J. Am. Chem. Soc.* **2006**, *128*, 10568−10571.

(3) Sun, X.; Zaric, S.; Daranciang, D.; Welsher, K.; Lu, Y.; Li, X.; Dai, H. Optical properties of ultrashort semiconducting single-walled carbon nanotube capsules down to sub-10 nm. *J. Am. Chem. Soc.* **2008**, *130*, 6551−6555.

DOI: 10.1021/acs.chemmater.9b01196
Chem. Mater. 2019, 31, 4536−4544

(4) Tabakman, S. M.; Welsher, K.; Hong, G.; Dai, H. Optical Properties of Single-Walled Carbon Nanotubes Separated in a Density Gradient; Length, Bundling, and Aromatic Stacking Effects. *J. Phys. Chem. C* **2010**, *114*, 19569−19575.
(5) Gao, Z.; Oudjedi, L.; Faes, R.; Morote, F.; Jaillet, C.; Poulin, P.; Lounis, B.; Cognet, L. Optical detection of individual ultra-short carbon nanotubes enables their length characterization down to 10 nm. *Sci. Rep.* **2015**, *5*, No. 17093.
(6) Danne, N.; Kim, M.; Godin, A. G.; Kwon, H.; Gao, Z.; Wu, X.; Hartmann, N. F.; Doorn, S. K.; Lounis, B.; Wang, Y.; Cognet, L. Ultrashort Carbon Nanotubes That Fluoresce Brightly in the Near-Infrared. *ACS Nano* **2018**, *12*, 6059−6065.
(7) Kuang, Y.; Liu, J.; Sun, X. Ultrashort Single-Walled Carbon Nanotubes: Density Gradient Separation, Optical Property, and Mathematical Modeling Study. *J. Phys. Chem. C* **2012**, *116*, 24770−24776.
(8) Rajan, A.; Strano, M. S.; Heller, D. A.; Hertel, T.; Schulten, K. Length-dependent optical effects in single walled carbon nanotubes. *J. Phys. Chem. B* **2008**, *112*, 6211−6213.
(9) Fagan, J. A.; Simpson, J. R.; Bauer, B. J.; Lacerda, S. H.; Becker, M. L.; Chun, J.; Migler, K. B.; Walker, A. R.; Hobbie, E. K. Length-dependent optical effects in single-wall carbon nanotubes. *J. Am. Chem. Soc.* **2007**, *129*, 10607−10612.
(10) Smith, A. M.; Mancini, M. C.; Nie, S. Bioimaging: second window for in vivo imaging. *Nat. Nanotechnol.* **2009**, *4*, 710−711.
(11) Welsher, K.; Liu, Z.; Sherlock, S. P.; Robinson, J. T.; Chen, Z.; Daranciang, D.; Dai, H. A route to brightly fluorescent carbon nanotubes for near-infrared imaging in mice. *Nat. Nanotechnol.* **2009**, *4*, 773−780.
(12) Godin, A. G.; Varela, J. A.; Gao, Z.; Danne, N.; Dupuis, J. P.; Lounis, B.; Groc, L.; Cognet, L. Single-nanotube tracking reveals the nanoscale organization of the extracellular space in the live brain. *Nat. Nanotechnol.* **2017**, *12*, 238−243.
(13) Yudasaka, M.; Yomogida, Y.; Zhang, M.; Tanaka, T.; Nakahara, M.; Kobayashi, N.; Okamatsu-Ogura, Y.; Machida, K.; Ishihara, K.; Saeki, K.; Kataura, H. Near-Infrared Photoluminescent Carbon Nanotubes for Imaging of Brown Fat. *Sci. Rep.* **2017**, *7*, No. 44760.
(14) Antaris, A. L.; Robinson, J. T.; Yaghi, O. K.; Hong, G.; Diao, S.; Luong, R.; Dai, H. Ultra-low doses of chirality sorted (6,5) carbon nanotubes for simultaneous tumor imaging and photothermal therapy. *ACS Nano* **2013**, *7*, 3644−3652.
(15) Iverson, N. M.; Barone, P. W.; Shandell, M.; Trudel, L. J.; Sen, S.; Sen, F.; Ivanov, V.; Atolia, E.; Farias, E.; McNicholas, T. P.; Reuel, N.; Parry, N. M.; Wogan, G. N.; Strano, M. S. In vivo biosensing via tissue-localizable near-infrared-fluorescent single-walled carbon nanotubes. *Nat. Nanotechnol.* **2013**, *8*, 873−880.
(16) Weinberger, B.; Heck, D. E.; Laskin, D. L.; Laskin, J. D. Nitric oxide in the lung. *Pharmacol. Ther.* **1999**, *84*, 401−411.
(17) Kolosnjaj-Tabi, J.; Hartman, K. B.; Boudjemaa, S.; Ananta, J. S.; Morgant, G.; Szwarc, H.; Wilson, L. J.; Moussa, F. In vivo behavior of large doses of ultrashort and full-length single-walled carbon nanotubes after oral and intraperitoneal administration to Swiss mice. *ACS Nano* **2010**, *4*, 1481−1492.
(18) Antaris, A. L.; Chen, H.; Cheng, K.; Sun, Y.; Hong, G.; Qu, C.; Diao, S.; Deng, Z.; Hu, X.; Zhang, B.; Zhang, X.; Yaghi, O. K.; Alamparambil, Z. R.; Hong, X.; Cheng, Z.; Dai, H. A small-molecule dye for NIR-II imaging. *Nat. Mater.* **2016**, *15*, 235−242.
(19) Kostarelos, K. The long and short of carbon nanotube toxicity. *Nat. Biotechnol.* **2008**, *26*, 774−776.
(20) Kamalasanan, K.; Gottardi, R.; Tan, S.; Chen, Y.; Godugu, B.; Rothstein, S.; Balazs, A. C.; Star, A.; Little, S. R. "Zero-dimensional" single-walled carbon nanotubes. *Angew. Chem., Int. Ed.* **2013**, *52*, 11308−11312.
(21) Piao, Y.; Meany, B.; Powell, L. R.; Valley, N.; Kwon, H.; Schatz, G. C.; Wang, Y. Brightening of carbon nanotube photoluminescence through the incorporation of sp3 defects. *Nat. Chem.* **2013**, *5*, 840−845.
(22) Kwon, H.; Furmanchuk, A.; Kim, M.; Meany, B.; Guo, Y.; Schatz, G. C.; Wang, Y. Molecularly Tunable Fluorescent Quantum Defects. *J. Am. Chem. Soc.* **2016**, *138*, 6878−6885.
(23) Brozena, A. K.; M, J.; Powell, L. R.; Wang, Y. H. Controlling the optical properties of carbon nanotubes with organic color-center quantum defects. *Nat. Rev. Chem.* **2019**, DOI: 10.1038/s41570-019-0103-5.
(24) Williams, R. M.; Lee, C.; Galassi, T. V.; Harvey, J. D.; Leicher, R.; Sirenko, M.; Dorso, M. A.; Shah, J.; Olvera, N.; Dao, F.; Levine, D. A.; Heller, D. A. Noninvasive ovarian cancer biomarker detection via an optical nanosensor implant. *Sci. Adv.* **2018**, *4*, No. eaaq1090.
(25) Vichchulada, P.; Cauble, M. A.; Abdi, E. A.; Obi, E. I.; Zhang, Q.; Lay, M. D. Sonication Power for Length Control of Single-Walled Carbon Nanotubes in Aqueous Suspensions Used for 2-Dimensional Network Formation. *J. Phys. Chem. C* **2010**, *114*, 12490−12495.
(26) Ziegler, K. J.; Gu, Z.; Peng, H.; Flor, E. L.; Hauge, R. H.; Smalley, R. E. Controlled oxidative cutting of single-walled carbon nanotubes. *J. Am. Chem. Soc.* **2005**, *127*, 1541−1547.
(27) Shuba, M. V.; Paddubskaya, A. G.; Kuzhir, P. P.; Maksimenko, S. A.; Ksenevich, V. K.; Niaura, G.; Seliuta, D.; Kasalynas, I.; Valusis, G. Soft cutting of single-wall carbon nanotubes by low temperature ultrasonication in a mixture of sulfuric and nitric acids. *Nanotechnology* **2012**, *23*, No. 495714.
(28) Kuznetsova, A.; Popova, I.; Yates, J. T.; Bronikowski, M. J.; Huffman, C. B.; Liu, J.; Smalley, R. E.; Hwu, H. H.; Chen, J. G. G. Oxygen-containing functional groups on single-wall carbon nanotubes: NEXAFS and vibrational spectroscopic studies. *J. Am. Chem. Soc.* **2001**, *123*, 10699−10704.
(29) Wu, X. J. K.; M, J.; Qu, H.; Wang, Y. H. Single-defect spectroscopy in the shortwave infrared. *Nat. Commun.* **2019**, DOI: 10.1038/s41467-019-10788-8.
(30) Frisch, M. J.; T, G. W.; Schlegel, H. B.; Scuseria, G. E.; Robb, M. A.; Cheeseman, J. R.; Scalmani, G.; Barone, V.; Mennucci, B.; Petersson, G. A. et al. *Gaussian 09*; Gaussian, Inc.: Wallingford, CT, 2009.
(31) Reed, A. E.; Weinstock, R. B.; Weinhold, F. Natural population analysis. *J. Chem. Phys.* **1985**, *83*, 735−746.
(32) Hudson, J. L.; Casavant, M. J.; Tour, J. M. Water-soluble, exfoliated, nonroping single-wall carbon nanotubes. *J. Am. Chem. Soc.* **2004**, *126*, 11158−11159.
(33) Kim, M.; Wu, X.; Ao, G.; He, X.; Kwon, H.; Hartmann, N. F.; Zheng, M.; Doorn, S. K.; Wang, Y. Mapping Structure-Property Relationships of Organic Color Centers. *Chem* **2018**, *4*, 2180−2191.
(34) Allen, B. L.; Kotchey, G. P.; Chen, Y.; Yanamala, N. V.; Klein-Seetharaman, J.; Kagan, V. E.; Star, A. Mechanistic investigations of horseradish peroxidase-catalyzed degradation of single-walled carbon nanotubes. *J. Am. Chem. Soc.* **2009**, *131*, 17194−17205.
(35) Wang, Y.; Shan, H.; Hauge, R. H.; Pasquali, M.; Smalley, R. E. A highly selective, one-pot purification method for single-walled carbon nanotubes. *J. Phys. Chem. B* **2007**, *111*, 1249−1252.
(36) García-Lastra, J. M.; Thygesen, K. S.; Strange, M.; Rubio, A. Conductance of sidewall-functionalized carbon nanotubes: universal dependence on adsorption sites. *Phys. Rev. Lett.* **2008**, *101*, No. 236806.
(37) Lopez-Bezanilla, A.; Triozon, F.; Latil, S.; Blase, X.; Roche, S. Effect of the chemical functionalization on charge transport in carbon nanotubes at the mesoscopic scale. *Nano Lett.* **2009**, *9*, 940−944.
(38) Dresselhaus, M. S.; Jorio, A.; Saito, R. Characterizing Graphene, Graphite, and Carbon Nanotubes by Raman Spectroscopy. *Annu. Rev. Condens. Matter Phys.* **2010**, *1*, 89−108.
(39) Ziegler, K. J.; Gu, Z.; Shaver, J.; Chen, Z.; Flor, E. L.; Schmidt, D. J.; Chan, C.; Hauge, R. H.; Smalley, R. E. Cutting single-walled carbon nanotubes. *Nanotechnology* **2005**, *16*, S539−544.
(40) Schöppler, F.; Mann, C.; Hain, T. C.; Neubauer, F. M.; Privitera, G.; Bonaccorso, F.; Chu, D.; Ferrari, A. C.; Hertel, T. Molar Extinction Coefficient of Single-Wall Carbon Nanotubes. *J. Phys. Chem. C* **2011**, *115*, 14682−14686.
(41) Streit, J. K.; Bachilo, S. M.; Ghosh, S.; Lin, C. W.; Weisman, R. B. Directly measured optical absorption cross sections for structure-

DOI: 10.1021/acs.chemmater.9b01196
Chem. Mater. 2019, 31, 4536−4544

selected single-walled carbon nanotubes. *Nano Lett.* **2014**, *14*, 1530−1536.
(42) Naumov, A. V.; Ghosh, S.; Tsyboulski, D. A.; Bachilo, S. M.; Weisman, R. B. Analyzing absorption backgrounds in single-walled carbon nanotube spectra. *ACS Nano* **2011**, *5*, 1639−1648.
(43) Venema, L. C. Imaging Electron Wave Functions of Quantized Energy Levels in Carbon Nanotubes. *Science* **1999**, *283*, 52−55.
(44) Hertel, T.; Himmelein, S.; Ackermann, T.; Stich, D.; Crochet, J. Diffusion limited photoluminescence quantum yields in 1-D semiconductors: single-wall carbon nanotubes. *ACS Nano* **2010**, *4*, 7161−7168.

DOI: 10.1021/acs.chemmater.9b01196
Chem. Mater. 2019, 31, 4536−4544